Supplementary Material: Dark spin-cats as biased qubits

Andreas Kruckenhauser,[1,2,3,*] Ming Yuan,[4,*] Han Zheng,[4,*] Mikhail Mamaev,[4] Pei Zeng,[4] Xuanhui Mao,[4] Qian Xu,[4] Torsten V. Zache,[1,2] Liang Jiang,[4] Rick van Bijnen,[1,2,3] and Peter Zoller[1,2]

[1] *Institute for Theoretical Physics, University of Innsbruck, 6020 Innsbruck, Austria*
[2] *Institute for Quantum Optics and Quantum Information of the Austrian Academy of Sciences, 6020 Innsbruck, Austria*
[3] *PlanQC GmbH, 85748 Garching, Germany*
[4] *Pritzker School of Molecular Engineering, University of Chicago, Chicago, Illinois 60637, USA*

(Dated: June 27, 2025)

In this Supplementary Material we provide further background material to the manuscript 'Dark spin-cats as biased qubits'. We provide derivations of key formulas and details of numerical simulations whose results are presented in the main-text.

CONTENTS

* These authors contributed equally.

I. SPIN COHERENT STATES AS THE DARK STATES OF THE DRIVING HAMILTONIAN

In this Section we review the derivation of the system Hamiltonian from Eq. (1) and provide a detailed derivation of the system dark sates (DSs).

A. System Hamiltonian

Here we review the derivation of the system Hamiltonian. The system we consider in the main-text is composed of two light coupled spin manifolds of length F_g and $F_e = F_g - 1$, respectively. The corresponding spin states are denoted by $|F_g,\, m\rangle$ and $|F_e,\, m\rangle$. The atomic level structure, see Fig. 1(e), is given by an overall manifold splitting ω_{eg}, with further magnetic substructure. In the presence of a static magnetic field $\mathbf{B}$ (defining the quantisation axis) the magnetic sublevels within a spin-manifold of states are split by the Zeeman shift $\delta_{g/e} = g_{g/e}\mu_B|\mathbf{B}|$, where $g_{g/e}$ is the manifold specific Landé-g factor and μ_B the Bohr magneton. The system Hamiltonian is given in the laboratory frame by

$$\hat{H}^{\rm lab}_{\rm DS}/\hbar = \omega_{eg}\hat{P}_e + \delta_e\hat{F}_{e,z} + \delta_g\hat{F}_{g,z} + \frac{1}{2}\sum_{q=0,\pm1}\left(e^{-i\omega_q t}\Omega^q\hat{\mathcal{C}}_q + {\rm h.c.}\right), \tag{1}$$

where the operator $\hat{P}_e = \sum_m |F_e, m\rangle\langle F_e, m|$ is a projector onto the excited manifold of states, and where ω_q and Ω^q denotes the oscillation and Rabi frequency of the light field with polarization $q \in \{\pm1,\, 0\}$, respectively. Note, the Rabi frequency Ω^q is a contravariant vector $\Omega^q = (\Omega_q)^*$, where Ω_q is the corresponding covariant vector [1], and the total Rabi frequency is given by $|\mathbf{\Omega}| = \sqrt{\sum_q \Omega^q\Omega_q}$. Furthermore, the coupling between the two spin manifolds is given by the operator $\hat{\mathcal{C}}_q = \sum_m \mathcal{C}^{F_e,m+q}_{F_g,m;1,q}|F_e, m+q\rangle\langle F_g, m|$, where

$$\mathcal{C}^{F_e,m+q}_{F_g,m;1,q} = \langle F_g, m; 1, q\,|F_e, m+q\rangle = \sqrt{2F_e+1}\frac{\langle F_e, m+q|\hat{T}^{(1)}_q|F_g, m\rangle}{\langle F_e||\hat{T}^{(1)}||F_g\rangle} \tag{2}$$

is a Clebsch-Gordan coefficient $\langle F_g, m_F; 1, q\,|F_e, m_F+q\rangle$, which, according to the Wigner-Eckart Theorem [2], is given by the transition matrix element of a spherical tensor $\hat{T}^{(k)}_q$ of rank $k = 1$ (due to the electric/magnetic dipole coupling) and the corresponding reduced matrix element $\langle F_g||\hat{T}^{(1)}||F_e\rangle$.

If the oscillation frequencies of the three light fields fulfill the Raman resonance criteria $\omega_q - \omega_{q'} = \delta_g(q-q')$, there exists a rotating frame transformation

$$\hat{\mathcal{U}} = \exp\left\{i\left[\omega_0\hat{P}_e + \delta_g(\hat{F}_{e,z} + \hat{F}_{g,z})\right]t\right\} \tag{3}$$

for which $\hat{H}^{\rm lab}_{\rm DS}$ becomes time-independent

$$\begin{aligned}\hat{H}_{\rm DS} &= \hat{\mathcal{U}}\,\hat{H}^{\rm lab}_{\rm DS}\,\hat{\mathcal{U}}^\dagger - i\hbar\hat{\mathcal{U}}(\partial_t\hat{\mathcal{U}}^\dagger)\\ &= -(\hbar\Delta\hat{P}_e + \hbar\delta\hat{F}_{e,z}) + \frac{1}{2}\sum_{q=0,\pm1}\left(\hbar\,\Omega^q\hat{\mathcal{C}}_q + {\rm h.c.}\right),\end{aligned} \tag{4}$$

with the detunings $\delta = \delta_g - \delta_e$ and $\Delta = \omega_0 - \omega_{eg}$. This Hamiltonian is equivalent to the Hamiltonian from the main-text Eq. (1).

B. Dark states

In the following we present a method to find the two DSs $|{\rm DS}_{1,2}\rangle$ of $\hat{H}_{\rm DS}$ from Eq. (4), which satisfy $\hat{H}_{\rm DS}|{\rm DS}_{1,2}\rangle = 0$. This DSs are fully encoded in the F_g-manifold of states and are thus insensitive to spontaneous emission from the excited states and also to the precises values of δ and Δ. If $|\mathbf{\Omega}| \neq 0$ the number of DSs is always given by 2 [3]. A result of this method is that the two DSs of $\hat{H}_{\rm DS}$ live in a Hilbert space spanned by two spin coherent states (SCSs) (up to a singular hyper parameter space), which are not necessarily orthogonal.

From a pedagogical point of view it is useful to first discuss three simple special cases and then describe the more general method.

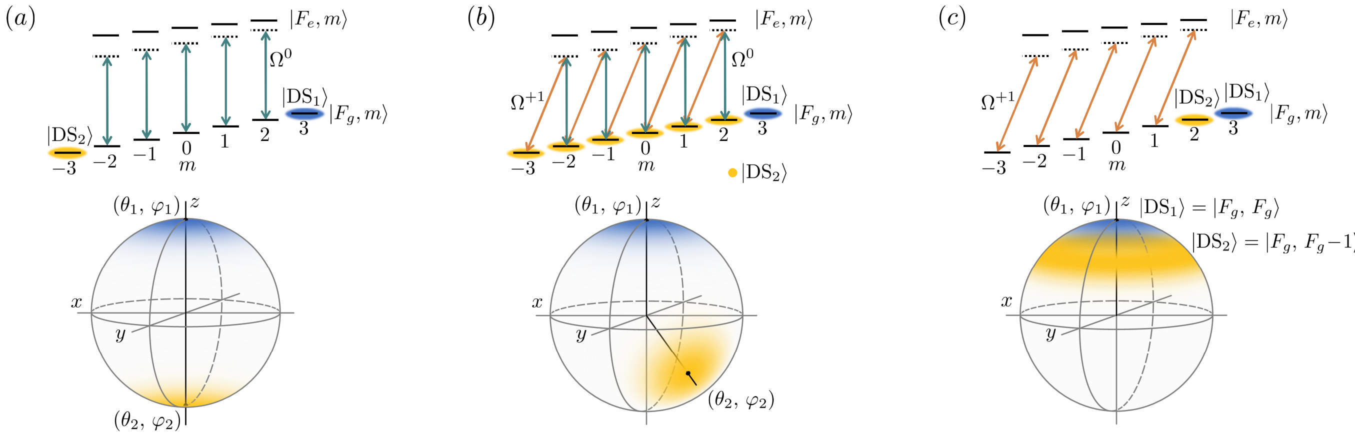

FIG. 1. Panels (a) - (c) Light coupling schemes, DSs and Wigner distributions for the three different examples discussed in the appendix section I B for $F_g = 3$.

1. We first focus on the case $\Omega^{\pm 1} = 0$ and $\Omega^0 = \Omega$, for which the two maximally stretched states $|\mathrm{DS}_{1,2}\rangle = |F_g,\, m = \pm F_g\rangle$ are not coupled by the light field and are thus the DSs of the system, see Fig. 1(a). Furthermore, the two maximally stretched states $|F_g,\, F_g\rangle = |\theta = 0,\, \varphi = 0\rangle$ and $|F_g,\, -F_g\rangle = |\theta = \pi,\, \varphi = 0\rangle$ are SCSs pointing along the $\pm z$-axis of the generalised F_g Bloch sphere. Hence, the DSs are given by two orthogonal SCSs.

2. Secondly, we consider the situation $\Omega^{-1} = 0$ and $\Omega^0 = \Omega^{+1} = \Omega/\sqrt{2}$, for which only the maximally stretched state $|\mathrm{DS}_1\rangle = |F_g,\, F_g\rangle$ is uncoupled and, therefore, is one of the two DSs, see Fig. 1(b). $|\mathrm{DS}_2\rangle$ is a superposition of states $|F_g,\, m\rangle$, with $m < F_g$. We will show below that $|\mathrm{DS}_2\rangle$ is given by a SCS, which has to be Schmidt orthogonlized with respect to $|\mathrm{DS}_1\rangle$. Thus, the Hilbert space spanned by $|\mathrm{DS}_1\rangle$ and $|\mathrm{DS}_2\rangle$ is equivalent to the one spanned by two non-orthogonal SCSs.

3. An example of the above mentioned single hyper parameter space is $\Omega^{+1} = \Omega$ and $\Omega^{-1} = \Omega^0 = 0$. Here the DSs can not be expressed by two SCSs as illustrated in Fig. 1(c). Insted, they are given by $|\mathrm{DS}_1\rangle = |F_g,\, F_g\rangle$ and $|\mathrm{DS}_2\rangle = |F_g,\, F_g{-}1\rangle$, where only $|\mathrm{DS}_1\rangle$ is a SCS.

The method we present in the following is based on spatial rotations $\hat{\mathcal{R}}$ such that the vector of Rabi frequencies $\boldsymbol{\Omega} = (\Omega^{+1},\, \Omega^0,\, \Omega^{-1})^{\mathrm{T}}$ in the rotated coordinate system $\boldsymbol{\Omega} \overset{\hat{\mathcal{R}}}{\to} \widetilde{\boldsymbol{\Omega}}$ obeys $\widetilde{\Omega}^{-1} = 0$. If this condition is fulfilled we can identify one of the two DSs (see example 2 from above) as the maximally stretched state $|F_g,\, F_g\rangle_{\widetilde{z}}$ along the $\widetilde{z}$-axis of the transformed coordinate system. The second SCS can be obtained by another rotation $\hat{\mathcal{R}}'$ for which $\widetilde{\Omega}'^{-1} = 0$ is satisfied and $|\mathrm{DS}_2\rangle$ can be obtained by a Schmidt orthogonalization with respect to $|\mathrm{DS}_1\rangle$.

To formalize this method we now discuss properties of $\hat{H}_{\mathrm{DS}}$ from Eq. (4) under spatial rotations

$$\hat{\mathcal{R}}(\alpha, \beta, \gamma) = e^{-i\alpha\left(\hat{F}_{g,z}+\hat{F}_{e,z}\right)} e^{-i\beta\left(\hat{F}_{g,y}+\hat{F}_{e,y}\right)} e^{-i\gamma\left(\hat{F}_{g,z}+\hat{F}_{e,z}\right)}, \tag{5}$$

where α, β and γ are extrinsic Euler angles. Under such a rotation H_{DS} becomes

$$\hat{\mathcal{R}}^\dagger \hat{H}_{\mathrm{DS}} \hat{\mathcal{R}}\, \frac{\langle F_e || \hat{T}^{(1)} || F_g\rangle}{\sqrt{2F_e+1}}\, \frac{1}{\hbar} \overset{\delta=\Delta=0}{\equiv} \sum_{m,m'} \hat{\mathcal{R}}^\dagger |F_e, m'\rangle\langle F_e, m'|\hat{\mathcal{R}} \left(\sum_q \Omega^q \left[\hat{\mathcal{R}}^\dagger \hat{T}^{(1)}_q \hat{\mathcal{R}}\right] \right) \hat{\mathcal{R}}^\dagger |F_g, m\rangle\langle F_g, m|\hat{\mathcal{R}} + \text{h.c.}, \tag{6}$$

where we expressed the CL coefficients in terms of $\hat{T}^{(1)}_q$ using Eq. (2). Note, as the DSs are independent of δ and Δ we dropped the detuning terms in Eq. (4) out of simplicity. Exploiting the transformation properties of spherical tensor operators [2] the inner bracket of the above equation can be rewritten as

$$\sum_q \Omega^q \left[\hat{\mathcal{R}}^\dagger \hat{T}^{(1)}_q \hat{\mathcal{R}}\right] = \sum_q \Omega^q \sum_{q'} D^{(1)*}_{q,q'}\, \hat{T}^{(1)}_{q'}, \tag{7}$$

where $D^{(1)}$ is the Wigner D-matrix, whose elements are given

$$D^{(1)}_{q,q'} = e^{-iq\alpha} d^{(1)}_{q,q'} e^{-iq'\gamma} \tag{8}$$

in terms of the small Wigner d-matrix

$$d^{(1)} = \begin{pmatrix} \frac{1+\cos\beta}{2} & -\frac{\sin\beta}{\sqrt{2}} & \frac{1-\cos\beta}{2} \\ \frac{\sin\beta}{\sqrt{2}} & \cos\beta & -\frac{\sin\beta}{\sqrt{2}} \\ \frac{1-\cos\beta}{2} & \frac{\sin\beta}{\sqrt{2}} & \frac{1+\cos\beta}{2} \end{pmatrix} \begin{bmatrix} +1 \\ 0 \\ -1 \end{bmatrix}. \tag{9}$$

From the transformation properties of the spherical tensor operators we identify the transformed coupling strengths as

$$\widetilde{\Omega}^{q'} = \sum_q \Omega^q D^{(1)*}_{q,q'} \tag{10}$$

As discussed above we are interested in rotations for which $\widetilde{\Omega}^{-1} = 0$. The rotation angles can be extracted from the solution of the following trigonometric equation

$$\widetilde{\Omega}^{-1} = e^{i\alpha}\left(\frac{1-\cos\beta}{2}\right)\Omega^{+1} - \frac{\sin\beta}{\sqrt{2}}\Omega^0 + e^{-i\alpha}\left(\frac{1+\cos\beta}{2}\right)\Omega^{-1} = 0, \tag{11}$$

where we dropped the γ term as this only adds a global phase (for the remainder we take without loss of generality $\gamma = 0$). In general, $\widetilde{\Omega}^{-1} = 0$ for two distinct rotations $\hat{\mathcal{R}}(\alpha_{1,2}, \beta_{1,2}, 0)$. The SCSs spanning the DS subspace are given by

$$|\theta_{1,2} = \beta_{1,2},\, \varphi_{1,2} = \alpha_{1,2}\rangle = \hat{\mathcal{R}}(\alpha_{1,2}, \beta_{1,2}, 0)|F_g,\, F_g\rangle. \tag{12}$$

Note, the definition here differs to the definition of Radcliffe [4] by $|\theta, \varphi\rangle = e^{-iF\varphi}|\theta, \varphi\rangle_{\text{Radcliffe}}$. Two orthogonal DSs can, for instance, be defined as

$$\begin{aligned} |\text{DS}_1\rangle &= |\theta_1,\, \varphi_1\rangle \\ |\text{DS}_2\rangle &= \left(|\theta_2,\, \varphi_2\rangle - \langle\theta_1,\, \varphi_1|\theta_2,\, \varphi_2\rangle|\theta_1,\, \varphi_1\rangle\right) / \sqrt{1 - |\langle\theta_1,\, \varphi_1|\theta_2,\, \varphi_2\rangle|^2}, \end{aligned} \tag{13}$$

where we Schmidt orthogonalized $|\text{DS}_2\rangle$ with respect to $|\text{DS}_1\rangle$.

The method discussed above gives to orthogonal DSs only when the tuples of angles are distinct, *i.e.* $(\theta_1,\, \varphi_1) \neq (\theta_2,\, \varphi_2)$. For $(\theta_1,\, \varphi_1) = (\theta_2,\, \varphi_2)$ the Rabi frequencies $\widetilde{\Omega}^q$ in the rotated coordinate system not only give $\widetilde{\Omega}^{-1} = 0$ but also $\widetilde{\Omega}^0 = 0$. For this special case, see example 3 from above, the two states in the rotated coordinate system $|F_g,\, F_g\rangle_{\tilde{z}}$ and $|F_g,\, F_g - 1\rangle_{\tilde{z}}$ are not coupled by the light field. Hence, the two DSs can not be expressed by two SCS, and can instead be chosen as $|\text{DS}_1\rangle = \hat{\mathcal{R}}(\alpha_1, \beta_1, 0)|F_g,\, F_g\rangle$ and $|\text{DS}_2\rangle = \hat{\mathcal{R}}(\alpha_1, \beta_1, 0)|F_g,\, F_g - 1\rangle$. Note, regardless of the specific vales of $(\theta_1,\, \varphi_1)$ and $(\theta_2,\, \varphi_2)$ it is always possible to define two DS with a well defined parity. That is, one DS only occupies even and the other DS only odd m Zeeman-levels, respectively.

Let us finally discuss the special situation where the two SCSs are orthogonal. This situation arises if the Cartesian components of the Rabi frequency (in the rotating frame defined by $\hat{\mathcal{U}}$)

$$\Omega^x = \frac{1}{\sqrt{2}}(\Omega^{-1} - \Omega^{+1}),\ \Omega^y = \frac{i}{\sqrt{2}}(\Omega^{-1} + \Omega^{+1}),\ \text{and}\ \Omega^z = \Omega^0 \tag{14}$$

are up to a global phase real numbers. Under these conditions the Cartesian Rabi frequency vector $\boldsymbol{\Omega} = (\Omega^x,\, \Omega^y,\, \Omega^z)$ defines the $\tilde{z}$-axis of the rotated coordinate system. Therefore, the rotation angles of $\hat{\mathcal{R}}(\alpha,\, \beta,\, 0)$ are given by

$$\begin{aligned} \alpha &= \text{sgn}(\Omega^y) \arccos\left[\frac{\Omega^x}{\sqrt{(\Omega^x)^2 + (\Omega^y)^2}}\right], \text{ and} \\ \beta &= \arccos\left[\frac{\Omega^z}{\sqrt{(\Omega^x)^2 + (\Omega^y)^2 + (\Omega^z)^2}}\right] \end{aligned} \tag{15}$$

for which $\widetilde{\Omega}^{\pm 1} = 0$ and $\widetilde{\Omega}^0 = \Omega$ and the DSs can be identified as the maximally polarized states $|F_g,\, \pm F_g\rangle_{\tilde{z}}$, as discussed in example 1 from above. A possible choice of DSs in this situation is $|\text{DS}_1\rangle = \hat{\mathcal{R}}(\alpha,\, \beta,\, 0)|F_g,\, F_g\rangle = |\beta, \alpha\rangle$ and $|\text{DS}_2\rangle = \hat{\mathcal{R}}(\alpha,\, \beta,\, 0)|F_g,\, -F_g\rangle = e^{-i\pi F_g}|\pi - \beta,\, \pi + \alpha\rangle$.

II. COLORED NOISE SIMULATION

Here we discuss the numerical methods used for simulating the system dynamics under colored noise used in the main-text to generate Figs. 1(c) and 3(a-d). For this, we consider a Markovian noise process $X(t)$ that couples to a system operator $\hat{\mathcal{O}}$, for example to $\hat{F}_{g,z}$ as considered in the main-text. The corresponding generalized multiplicative stochastic master equation is given by

$$\hbar\partial_t\hat{\rho}(t) = \hat{\mathcal{L}}\hat{\rho}(t) - i\left[\hbar\, X(t)\hat{\mathcal{O}}, \hat{\rho}(t)\right], \text{ with}$$
$$\hat{\mathcal{L}}\hat{\rho}(t) = -i\left[\hat{H},\, \rho(t)\right] + \hbar\sum_a \gamma_a \mathcal{D}\left[\hat{a}\right] \tag{16}$$

where $\hat{\mathcal{L}}$ is the system Lindbladian decomposed into a Hamiltonian part $\hat{H}$ and dissipative part described by jump operators $\hat{a}$, with rate γ_a and $\mathcal{D}[\hat{a}]\hat{\rho}(t) = \hat{a}\hat{\rho}(t)\hat{a}^\dagger - \frac{1}{2}\{\hat{a}^\dagger\hat{a}, \hat{\rho}(t)\}$. Importantly, $\hat{\rho}(t)$ denotes the density operator for a particular noise trajectory $X(t)$. The average density operator $\langle\hat{\rho}(t)\rangle_{\rm s}$, which is the quantity we wish to calculate, is defined by the statistical mean of $\hat{\rho}(t)$ over all possible noise trajectories $X(t)$. The noise trajectories are associated with a probability distribution $P(X,t)$, which satisfies a differential equation of the following form

$$\hbar\partial_t P(X,t) = \hat{\Lambda}\, P(X,t), \tag{17}$$

where $\hat{\Lambda}$ is called Fokker-Planck (differential-) operator for continuous noise models, or, a transition rate matrix for jump-like noise models, respectively. In the main-text we considered a Ornstein-Uhlenbeck (OU) process which will be detailed below.

The statistical mean $\langle\hat{\rho}(t)\rangle_{\rm s}$ can either be calculated by trajectory sampling or alternatively directly employing the concept of marginal densities. In the following we will summarize the relevant formula using the latter approach, where we closely follow Ref. [5]. The marginal density $\hat{u}(X,t)$, with elements $u_{\mu,\nu}(X,t)$, where μ,ν are the indices corresponding to the density operator element $\rho_{\mu,\nu}(t)$, is related to the statistical mean of the density operator by [6]

$$\langle\hat{\rho}(t)\rangle_{\rm s} = \int \hat{u}(X,t)\,\mathrm{d}X. \tag{18}$$

The differential equation which $\hat{u}(X,t)$ satisfies reads

$$\hbar\partial_t \left|u(X,t)\right\rangle\!\rangle = \left[\hat{\Lambda} - i\hbar X\hat{\hat{\mathcal{O}}} + \hat{\hat{\mathcal{L}}}\right]\left|u(X,t)\right\rangle\!\rangle\,, \tag{19}$$

where $|u(X,t)\rangle\!\rangle$ is a column stacked vectorization of $\hat{u}(X,t)$, and $\hat{\hat{\mathcal{O}}}$ and $\hat{\hat{\mathcal{L}}}$ are the associated column stacked super-operators. The initial state of the marginal densities is given by $\hat{u}(X,t=0) = P_{\rm ss}(X)\,\hat{\rho}(0)$, where $P_{\rm ss}(X)$ is the steady-state noise distribution, which satisfies $\hat{\Lambda}P_{\rm ss}(X) = 0$.

In the following we will provide explicit expressions of the super-operators for the colored noise simulations presented in the main-text. In the main-text we considered the OU process, whose Fokker-Planck operator is given by

$$\hat{\Lambda}/\hbar = \lambda\,\partial_X X + \sigma^2/2\,\partial_X^2, \tag{20}$$

where $1/\lambda$ and σ^2 determine the noise correlation time and diffusion constant, respectively [7]. In the main-text we introduced $\kappa = \sigma^2/\lambda^2$, which corresponds to the strength of the noise in the white noise limit. In particular, if λ is much larger (smaller) than the characteristic energy scale of $\hat{H}$, the noise effectively appears white (static), as discussed below.

The numerical integration of Eq. (19) requires a discretization of the continuous variable X onto N_X values. To do so, we use Eq. (6) from Ref. [8], for which the discretization of the Fokker-Planck equation reads

$$\hbar\partial_t\begin{pmatrix}P(X_{-1},\,t)\\ P(X_0,\,t)\\ P(X_{+1},\,t)\end{pmatrix} = \hat{\Lambda}_{N_X=3}\begin{pmatrix}P(X_{-1},\,t)\\ P(X_0,\,t)\\ P(X_{+1},\,t)\end{pmatrix} = \hbar\lambda\begin{pmatrix}-1 & \frac{1}{2} & 0\\ 1 & -1 & 1\\ 0 & \frac{1}{2} & -1\end{pmatrix}\begin{pmatrix}P(X_{-1},\,t)\\ P(X_0,\,t)\\ P(X_{+1},\,t)\end{pmatrix}, \tag{21}$$

and the discretized stochastic field can take on the values

$$\begin{pmatrix}X_{-1}\\ X_0\\ X_{+1}\end{pmatrix} = \sqrt{\kappa\lambda}\begin{pmatrix}-1\\ 0\\ 1\end{pmatrix}. \tag{22}$$

The associated steady state distribution is given by $P_{\rm ss} = (1/4,\,1/2,\,1/4)^T$.

For completeness we will state here explicitly the vectorization of Eq. (19) used for the main-text simulations. For the column stacked vectorization we follow Ref. [9]:

1. Coherent Dynamics

$$-i[\hat{H},\hat{\rho}] \Leftrightarrow -i\left(\mathbb{1}_n \otimes \hat{H} - \hat{H}^T \otimes \mathbb{1}_n\right)|\rho(t)\rangle\!\rangle = -i\hat{\hat{H}}\,|\rho(t)\rangle\!\rangle \tag{23}$$

2. Dissipative Dynamics

$$D[\hat{a}]\hat{\rho} \Leftrightarrow \left[(\hat{a}^\dagger)^T \otimes \hat{a} - \frac{1}{2}\left(\left(\hat{a}^\dagger\hat{a}\right)^T \otimes \mathbb{1}_n + \mathbb{1}_n \otimes \hat{a}^\dagger\hat{a}\right)\right]|\rho(t)\rangle\!\rangle = \hat{\hat{D}}[\hat{a}]\,|\rho(t)\rangle\!\rangle \tag{24}$$

Here, $\mathbb{1}_n$ is the identity operator on the n-dimensional system Hilbert space. Thus, the dynamics of the marginal densities is governed by

$$\hbar\partial_t\begin{pmatrix}|u(X_{-1},\,t)\rangle\!\rangle\\|u(X_0,\,t)\rangle\!\rangle\\|u(X_{+1},\,t)\rangle\!\rangle\end{pmatrix} = \left[\hat{\Lambda}_3 \otimes \mathbb{1}_{n^2} - i\hbar\sqrt{\kappa\lambda}\begin{pmatrix}-1&0&0\\0&0&0\\0&0&+1\end{pmatrix}\otimes\hat{\hat{O}} + \mathbb{1}_3 \otimes \left(-i\hat{\hat{H}} + \hbar\sum_a \gamma_a\hat{\hat{D}}[\hat{a}]\right)\right]\begin{pmatrix}|u(X_{-1},\,t)\rangle\!\rangle\\|u(X_0,\,t)\rangle\!\rangle\\|u(X_{+1},\,t)\rangle\!\rangle\end{pmatrix}. \tag{25}$$

The vectorized statistical average density operator is then calculated as $|\langle\rho(t)\rangle_{\mathrm{s}}\rangle\!\rangle = \sum_\alpha |u,\,X_\alpha\rangle\!\rangle$. Note, beside the finite discretization of the continuous noise process this approach is exact.

Finally we discuss the white noise limit of the OU process. The white noise limit corresponds to the limit when the noise correlation time $1/\lambda$ vanishes ($\lambda \to \infty$) and thus the noise process becomes uncorrelated. In particular, this can be seen by evaluating the steady state noise covariance function

$$\langle X(t)X(0)\rangle_{\mathrm{s}} - \langle X(t)\rangle_{\mathrm{s}}\langle X(0)\rangle_{\mathrm{s}} = \frac{\kappa\lambda}{2}e^{-\lambda t} \overset{\lambda\to\infty}{=} \kappa\delta(t). \tag{26}$$

Note, this analysis applies to the continuous and discretized OU process. The strength of the white noise process is determined by κ and the associated master equation reads

$$\hbar\partial_t\hat{\rho}(t) = -i[\hat{H},\hat{\rho}(t)] + \hbar\sum_a \gamma_a\mathcal{D}\left[\hat{a}\right]\hat{\rho}(t) + \hbar\kappa\mathcal{D}\big[\hat{O}\big]\hat{\rho}(t), \tag{27}$$

which is used for the white noise simulation presented in the main-text.

III. PAULI TRANSFER MATRIX

In the following section we discuss time-evolution of logical states using the Pauli transfer matrix (PTM) formalism. This formalism is used in the main-text to characterize the error channels, when the system is subject to colored noise processes and imperfect logical gate operations (described in subsequent sections).

A logical initial state, given by a density matrix $\hat{\rho}(t=0)$, can be expressed as

$$\hat{\rho}(0) = \left[d_0(0)\,\widetilde{\mathbb{1}} + \sum_{n\in\{\widetilde{x},\widetilde{y},\widetilde{z}\}} d_n(0)\hat{\sigma}_n\right]/2, \tag{28}$$

where $\widetilde{\mathbb{1}}$ and $\hat{\sigma}_{\widetilde{x}}$, $\hat{\sigma}_{\widetilde{y}}$, and $\hat{\sigma}_{\widetilde{z}}$ are the logical identity- and Pauli-operators, respectively, as defined in the main-text. Furthermore, $\boldsymbol{d}(0) = (d_{\widetilde{x}}(0),\, d_{\widetilde{y}}(0),\, d_{\widetilde{z}}(0))^{\mathrm{T}}$ is the three component logical Bloch sphere vector, with $|\boldsymbol{d}(0)| \le 1$. For completeness we also keep the fourth component $d_0(0)$, which describes leakage out of the logical subspace when $d_0(0) < 1$. Time evolution from $\hat{\rho}(0)$ to $\hat{\rho}(t)$ can be expressed as [10]

$$\hat{\rho}(t) = \left[d_0(t)\,\widetilde{\mathbb{1}} + \sum_{n\in\{\widetilde{x},\widetilde{y},\widetilde{z}\}} d_n(t)\hat{\sigma}_n\right]/2, \text{ with} \tag{29}$$

$$d_n(t) = \sum_m R_{n,m}(t)d_m(0), \tag{30}$$

where $R_{n,m}(t)$ is the PTM given by

$$R_{n,m}(t) = \frac{1}{2}\mathrm{tr}\left[\hat{E}_n\,\hat{\rho}_m(t)\right] \text{ for } \hat{\rho}_m(0) = \hat{E}_m, \tag{31}$$

and the operators $\hat{E}_n$ are defined as

$$
\begin{aligned}
\hat{E}_0 &= \widetilde{\mathbb{1}} = |\widetilde{0}\rangle\langle\widetilde{0}| + |\widetilde{1}\rangle\langle\widetilde{1}|, \\
\hat{E}_{\widetilde{x}} &= \hat{\sigma}_{\widetilde{x}} = |\widetilde{1}\rangle\langle\widetilde{0}| + |\widetilde{0}\rangle\langle\widetilde{1}|, \\
\hat{E}_{\widetilde{y}} &= \hat{\sigma}_{\widetilde{y}} = -i\left(|\widetilde{1}\rangle\langle\widetilde{0}| - |\widetilde{0}\rangle\langle\widetilde{1}|\right), \text{ and} \\
\hat{E}_{\widetilde{z}} &= \hat{\sigma}_{\widetilde{z}} = |\widetilde{1}\rangle\langle\widetilde{1}| - |\widetilde{0}\rangle\langle\widetilde{0}|.
\end{aligned}
\tag{32}
$$

The diagonal elements $R_{n,n}(t)$ decrease at a rate dependent on the noise strength and correlation time. A decrease of the diagonal elements of the PTM characterizes shrinkage of the Bloch vector, i.e. increases the mixedness of quantum state.

IV. AUTONOMOUS STABILIZATION

Here we detail the general theory employed for our autonomous stabilization protocol, that protect the logical qubit from the colored noise models discuss section II. We consider the laser coupling Hamiltonian from Eq. (4) with zero detunings and Rabi frequencies $\Omega^{+1} = -\Omega^{-1} = -\sqrt{2}\Omega$,

$$
\hat{H}_{\mathrm{DS}}/\hbar = -\frac{\Omega}{\sqrt{2}}\left(\hat{\mathcal{C}}_{+1} - \hat{\mathcal{C}}_{-1} + \text{h.c.}\right), \tag{33}
$$

for which the two DSs $\hat{H}_{\mathrm{DS}}|\mathrm{DS}_{1,2}\rangle = 0$ [corresponding to our logical qubit states from the main-text Eq. (2)] are,

$$
\begin{aligned}
|\mathrm{DS}_1\rangle &= |\widetilde{0}\rangle = e^{-i\frac{\pi}{2}\hat{F}_{g,y}}|F_g, +F_g\rangle = |F_g, +F_g\rangle_x \text{ and} \\
|\mathrm{DS}_2\rangle &= |\widetilde{1}\rangle = e^{-i\frac{\pi}{2}\hat{F}_{g,y}}|F_g, -F_g\rangle = |F_g, -F_g\rangle_x
\end{aligned}
\tag{34}
$$

according to Sec. I B. Here, $|F_g, m\rangle_x$ is a hyperfine state with angular momentum projection m along the x-axis of the Bloch sphere (rather than along the magnetic quantization axis). In addition to laser driving the F_e-manifold is subject to spontaneous emission [11], described by the following master equation

$$
\hbar\partial_t\hat{\rho}(t) = \hat{\mathcal{L}}_{\mathrm{stab}}\hat{\rho}(t) = -i[\hat{H}_{\mathrm{DS}}, \hat{\rho}(t)] + \hbar\gamma\sum_{q=0,\pm1}\mathcal{D}\left[\hat{\mathcal{C}}_q^\dagger\right]\hat{\rho}(t). \tag{35}
$$

As spontaneous emission only affects the F_e-manifold of states, the four operators $|\widetilde{0}\rangle\langle\widetilde{0}|$, $|\widetilde{1}\rangle\langle\widetilde{0}|$, $|\widetilde{0}\rangle\langle\widetilde{1}|$ and $|\widetilde{1}\rangle\langle\widetilde{1}|$ are the steady states of the system. Thus, in the limit of infinite time-evolution $t \to \infty$ under the above driven-dissipative system, any state $\hat{\rho}$ will relax to a density matrix spanning just the logical subspace, $\hat{\rho}_\infty \equiv \lim_{t\to\infty}\hat{\rho}(t)$ given by,

$$
\hat{\rho}_\infty = c_{00}|\widetilde{0}\rangle\langle\widetilde{0}| + c_{01}|\widetilde{0}\rangle\langle\widetilde{1}| + c_{10}|\widetilde{1}\rangle\langle\widetilde{0}| + c_{11}|\widetilde{1}\rangle\langle\widetilde{1}|. \tag{36}
$$

The coefficients $c_{\mu\nu}$ are determined by the overlap of the initial density matrix with the system's appropriate conserved quantities,

$$
c_{\mu\nu} = \mathrm{tr}\left[\hat{J}_{\mu\nu}^\dagger\hat{\rho}(0)\right], \tag{37}
$$

where $\hat{J}_{\mu\nu}$ are the left hand eigenvectors of the Liouvillian with eigenvalue zero

$$
\langle\langle J_{\mu\nu}|\hat{\hat{\mathcal{L}}}_{\mathrm{stab}} = 0, \tag{38}
$$

where $|A\rangle\rangle$ is a vectorized (columns stacked) version of an operator $\hat{A}$, and the corresponding Liouvillian super-operator matrix is defined via the master equation $\partial_t|\rho\rangle\rangle = \hat{\hat{\mathcal{L}}}_{\mathrm{stab}}|\rho\rangle\rangle$ [12].

The conserved quantities associated with the $\hat{\mathcal{L}}_{\mathrm{stab}}$ can be found analytically ($\delta = \Delta = 0$) in both integer and half-integer spin F_g,

$$
\begin{aligned}
\hat{J}_{00} &= |\widetilde{0}\rangle\langle\widetilde{0}| + \sum_{m=-F_g+1}^{F_g-1} a_m\Big(|F_g, m\rangle_x\langle F_g, m| + |F_e, m\rangle_x\langle F_e, m|\Big), \\
\hat{J}_{11} &= \mathbb{1} - \hat{J}_{00}, \\
\hat{J}_{01} &= |\widetilde{0}\rangle\langle\widetilde{1}|, \\
\hat{J}_{10} &= |\widetilde{1}\rangle\langle\widetilde{0}|,
\end{aligned}
\tag{39}
$$

with $\mathbb{1} = \sum_{m=-F_g}^{F_g} |F_g, m\rangle_x \langle F_g, m| + \sum_{m=-F_e}^{F_e} |F_e, m\rangle_x \langle F_e, m|$ is the identity operator. The coefficients a_m for $1 - F_g \leq m \leq F_g - 1$ satisfies

$$a_m = \frac{\sum_{m'=-F_g}^{m-1} G(m')}{\sum_{m'=-F_g}^{F_g-1} G(m')}, \text{ with}$$
$$G(m) = \begin{cases} \prod_{m'=-F_g+1}^{m} \frac{(F_g-m'+1)(F_g-m')}{(F_g+m'+1)(F_g+m')}, & -F_g + 1 \leq m \leq F_g - 1, \\ 1, & m = -F_g. \end{cases} \tag{40}$$

The denominator in the expression of a_m can be further evaluated as

$$\sum_{m'=-F_g}^{F_g-1} G(m') = {}_2F_1(-2F_g, 1 - 2F_g; 2; 1) = \frac{(4F_g)!}{(2F_g + 1)!(2F_g)!} \simeq \frac{16^{F_g}}{F_g^{3/2}\sqrt{8\pi}} \qquad (F_g \gg 1), \tag{41}$$

where ${}_2F_1(a, b; c; z)$ is the hypergeometric function, and the approximated expression in the end is achieved using Stirling's formula $n! \simeq \sqrt{2\pi n}(\frac{n}{e})^n$ under the large n limit.

With the knowledge of the conserved quantities, we can evaluate the action of the autonomous stabilization protocol following various logical operations without the need to explicitly evolve the master equation to long times. Whenever we employ stabilization (and no other non-negligible Hamiltonians or dissipators), we evaluate the effect by simply projecting the density matrix of the qubit into the logical subspace via Eqs. (36) and (37).

A. Biased effective error model

While we use a specific colored noise simulation to benchmark the 'dark spin-cat' against unwanted external noise, the exponential suppression of bit-flip errors in the cat size F_g emerges quite generically for *any* perturbation that acts locally in the basis of spin states, i.e. that changes angular momentum by only a few units at a time. As an example, we consider white noise generated by $\mathcal{D}[\sqrt{\kappa}\hat{F}_{g,z}]$. The conserved quantities $\hat{J}_{nm}$ can be used to derive the exponentially in F_g suppressed change of rate of the PTM, which is to leading first order in κ given by

$$\dot{R}_{\widetilde{z},\widetilde{z}} = -\kappa F_g a_{-(F_g-1)} \simeq -\kappa \frac{F_g^{5/2}\sqrt{8\pi}}{16^{F_g}}. \tag{42}$$

On the contrary, the logical dephasing error rate only amplifies by a factor of F_g. The effect of $\mathcal{D}[\sqrt{\kappa}\hat{F}_{g,y}]$ will be similar to $\mathcal{D}[\sqrt{\kappa}\hat{F}_{g,z}]$ due to the rotational symmetry along x direction. On the other hand, $\mathcal{D}[\sqrt{\kappa}\hat{F}_{g,x}]$ noise will not let the code states leave out of the encoded subspace but will give $|\widetilde{0}\rangle$, $|\widetilde{1}\rangle$ a relative phase, which leads to a dephasing error with the rate scales as $O(F_g^2)$.

As a practical aside, while the autonomous stabilization will always relax the qubit into the logical subspace in the limit $t \to \infty$, the rate of stabilization is set by the dissipative gap $\Delta_{\rm diss}$. This gap can be written as $\Delta_{\rm diss} = -\mathrm{Re}(\lambda_{\rm diss})$, where $\lambda_{\rm diss}$ is the right eigenvalue of the Liouvillian super-operator $\hat{\hat{\mathcal{L}}}_{\rm stab} |\lambda_{\rm diss}\rangle\!\rangle = \lambda_{\rm diss} |\lambda_{\rm diss}\rangle\!\rangle$, with the smallest non-zero real part. A larger $\Delta_{\rm diss}$ leads to faster stabilization. If the stabilization is active at the same time as an error process with magnitude κ is present, as considered in the main-text, the error will be suppressed provided $\kappa F_g \ll \Delta_{\rm diss}$. In our simulations, we consider the regime $|\boldsymbol{\Omega}| \gg \gamma$, where to numerical study suggests that dissipation gap satisfies $\Delta_{\rm diss} \simeq \gamma/(2F_g + 1)$, as shown in FIG. 2.

B. Numerical benchmark

Here we comment on the numerical simulation of the autonomous stabilization mechanism presented in the main-text. In particular, in the main-text Figs. 1(c) and 3(b), we present the time derivative of the diagonal elements of the PTM $\partial_t R_{n,n}(t)$ rather than the matrix elements themselves when subjected to a colored-noise process as discussed in Sec. II. Note, the element $R_{0,0}(t)$ describes leakage out of the logical qubit subspace and takes on for $\kappa t \to \infty$ a constant value close to unity, *i.e.* a balance between the leakage generating colored noise process and the autonomous stabilization mechanism.

For the main-text simulations we assumed the Landé-g factor of the F_g and F_e manifold of states are equal, thus we use $\delta = 0$ in the main-text Eq. (1). The actual value of δ depends on the specific atomic platform, the considered levels and also the applied magnetic field. In the following we will discuss the effect of such a non-zero δ. For the parameters chosen in the main-text below Eq. (2) ($\boldsymbol{\Omega} = (\Omega^x,\ 0,\ 0)^T$) the laser-coupling becomes particularly simple, see Fig. 3 (or main-text Fig. 3(a)). In

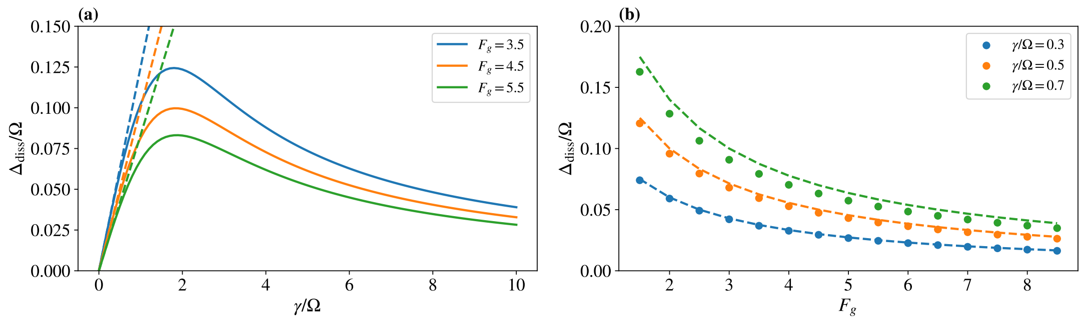

FIG. 2. Dissipation gap $\Delta_{\rm diss}$ varies as the change of spontaneous emission strength γ and spin length F_g. (a) Fixed F_g and varying γ. (b) Fixed γ and varying F_g. Dashed lines in both plots are references with $\Delta_{\rm diss} = \gamma/(2F_g + 1)$.

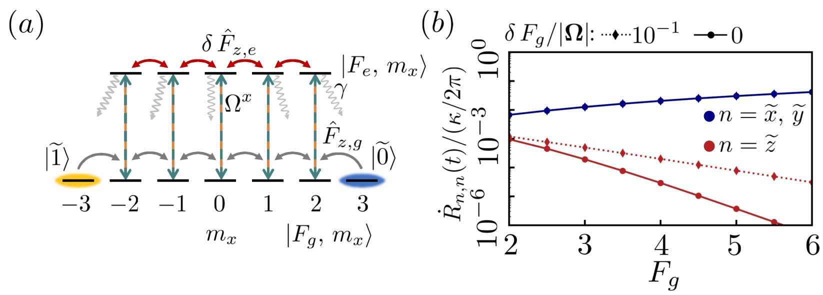

FIG. 3. (a) Illustration of laser coupling ($F_g = 3$) in the rotated coordinate system, for which $\mathbf{\Omega} = (\Omega^x,\, 0,\, 0)^T$ defines the quantization axis. Note, the detunings are taken in contrast to the main-text figure 3(a) to be $\Delta = 0$ and $\delta \neq 0$, which gives rise to an additional coupling in the F_e-manifold of states (red arrows). Spontaneous emission of $|F_e,\, m_x\rangle$ is due to the CG coefficients directed "towards" the closest DS, as illustrated by wavy arrows indicating the average m_x change. (b) Time derivative of the diagonal elements of $\mathbf{R}(t)$ as a function of F_g for different values of δ. Here $\Delta = 0$, $|\mathbf{\Omega}|/\gamma = 2\pi$, $F_g = 4$, $\kappa = 10^{-4}|\mathbf{\Omega}|$, $\lambda/|\mathbf{\Omega}| = 10^{-3}$ and $N_X = 3$.

this frame the differential shift $\delta\, F_{e,z}$ couples adjacent states in the F_e-manifold of states. This coupling alters the composition of the bright-states and, thus, disturbs the autonomous stabilization mechanism. In particular, the exponent of the exponentially suppressed bit-flip error rate $R_{\widetilde{z},\widetilde{z}}(t)$ is increased, whereas, the dephasing rates $R_{\widetilde{x},\widetilde{x}}(t)$ and $R_{\widetilde{y},\widetilde{y}}(t)$ are unaltered, see Fig. 3 (b). However, from numerical simulations we observe that there is still an exponential suppressed bit-flip error rate as compared to the dephasing-rate for $\delta\, F_g < |\mathbf{\Omega}|$, hence, the model-system still exhibits an exponentially in F_g biased error model.

C. Autonomous error correction with engineered dissipation

Above we discussed the ability of autonomous stabilization in the system we considered, i.e., when the population leaves the encoded subspace due to the perturbation from the noise, it will passively go back under the dissipative process. However, as indicated in the form of conserved quantities $\hat{J}_{01}$ and $\hat{J}_{10}$ shown in Eq. (39), if initially there is quantum coherence between $|\widetilde{0}\rangle$ and $|\widetilde{1}\rangle$, then such coherence will be totally lost when it leaves the code subspace and goes back again due to the stabilization. Therefore, the leakage will be converted to a dephasing error.

On the other hand, if we can select the polarization of the decay from excited levels to the ground, then certain noise like $\mathcal{D}[\sqrt{\kappa}\hat{F}_{g,z}]$ can be further corrected. The idea is to only keep the decay process with $\sigma_\pm$ polarization ($\Delta m_z = \pm 1$, see Fig. 4), which can be achieved by putting the atoms in a cavity [13]. In this way, the dissipative part in the master equation (35) should be modified to $\gamma \sum_{q=\pm 1} \mathcal{D}[\hat{\mathcal{C}}_q]\hat{\rho}(t)$. Now the parity operator $\hat{\Pi} = e^{i\pi(\hat{F}_{g,z} + \hat{F}_{e,z} + \hat{P}_e - F_g)}$ will be preserved during the evolution, so for noise like $\mathcal{D}[\sqrt{\kappa}\hat{F}_{g,z}]$ that does not affect the parity of the states, the coherence between $|\widetilde{0}\rangle$ and $|\widetilde{1}\rangle$ can also be mostly preserved, in contrast to the case where the excited manifold is subject to spontaneous decay. However, the dephasing error induced by $\mathcal{D}[\sqrt{\kappa}\hat{F}_{g,y}]$ will increase, as it will flip the parity of the code states while causing them to leave the encoded subspace.

Those features can also be illustrated with the analysis of conserved quantities under the new Lindbladian. In the strong driving limit ($\Omega \gg \gamma$), we can still write down the expressions for those conserved quantities to the 0-th order (up to $O[(\gamma/\Omega)^0]$)

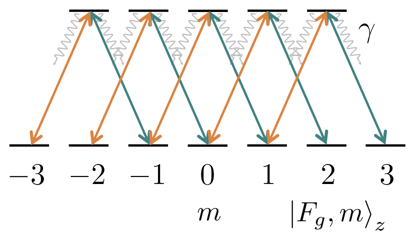

FIG. 4. Schematic plot for the engineered dissipation. When atoms are in a cavity, the decay may happen with two different polarizations rather than three. The system can be separated into two parts characterized by parity $\hat{\Pi}$, where there is no coupling between the two parts.

as the following:

$$\begin{aligned}
\hat{J}'_{00} &\simeq |\widetilde{0}\rangle\langle\widetilde{0}| + \sum_{m=-F_g+1}^{F_g-1} a_m \Big(|F_g, m\rangle_x \langle F_g, m| + |F_e, m\rangle_x \langle F_e, m| \Big), \\
\hat{J}'_{11} &= \mathbb{1} - \hat{J}'_{00}, \\
\hat{J}'_{01} &\simeq |\widetilde{0}\rangle\langle\widetilde{1}| + \sum_{m=-F_g+1}^{F_g-1} a_m \Big(|F_g, m\rangle_x \langle F_g, -m| + |F_e, m\rangle_x \langle F_e, -m| \Big), \\
\hat{J}'_{10} &= \hat{J}'^{\dagger}_{01}.
\end{aligned} \tag{43}$$

For a state $|\psi\rangle = a|\widetilde{0}\rangle + b|\widetilde{1}\rangle$, it will hop to $|\psi_1\rangle = a|F_g, F_g - 1\rangle_x + b|F_g, -(F_g - 1)\rangle_x$ when suffering from a jump operator $\hat{F}_{g,z}$. However, the difference between the overlap $\langle\psi|\hat{J}'_{01}|\psi\rangle$ and $\langle\psi_1|\hat{J}'_{01}|\psi_1\rangle$ is again exponentially suppressed with F_g, which indicates that the phase coherence between $|\widetilde{0}\rangle$ and $|\widetilde{1}\rangle$ can also be well preserved after the dissipative stabilization process. This observation, together with the bit-flip protection, provides a passive correction of the $\hat{F}_{g,z}$ error with the engineered dissipation.

V. NUMERICAL SIMULATIONS OF LOGICAL GATES

Here we detail the numerical simulations used to benchmark the adiabatic logical gates in the main-text Figure 3. The same colored-noise simulation described for $N_X = 3$ from above is employed, except the driving laser Rabi frequency phases and amplitudes are explicitly time-dependent. Therefore, we consider the generalised time-dependent Hamiltonian from Eq. (4), namely

$$\hat{H}_{\rm DS}(t)/\hbar = \frac{1}{2}\sum_{q=0,\pm1}\Big(\Omega^q(t)\hat{\mathcal{C}}_q + \text{h.c.}\Big) \tag{44}$$

From what will follow, it is convenient to parameterize the Rabi frequencies as follows

$$\begin{pmatrix}\Omega^{+1}\\ \Omega^0\\ \Omega^{-1}\end{pmatrix} = \Omega\begin{pmatrix}-\frac{1}{\sqrt{2}}e^{i\alpha(t)} & \sin[\beta(t)]\\ & \cos[\beta(t)]\\ \frac{1}{\sqrt{2}}e^{-i\alpha(t)} & \sin[\beta(t)]\end{pmatrix}, \tag{45}$$

with time dependent parameters $\alpha(t)$ and $\beta(t)$. The associated Cartesian components of the Rabi frequencies

$$\begin{aligned}
\Omega^x &= \Omega\cos[\alpha(t)]\sin[\beta(t)], \\
\Omega^y &= \Omega\sin[\alpha(t)]\sin[\beta(t)], \text{ and} \\
\Omega^z &= \Omega\cos[\beta(t)]
\end{aligned} \tag{46}$$

are by construction always real and, thus, the instantaneous DSs $|\text{DS}_{1,2}(t)\rangle$, satisfying $\hat{H}_{\rm DS}(t)|\text{DS}_{1,2}(t)\rangle = 0$, can always be identified with orthogonal SCSs, see Sec. I B

$$\begin{aligned}
|\text{DS}_1(t)\rangle &= \hat{\mathcal{R}}[\alpha(t), \beta(t), 0]\,|F_g, +F_g\rangle, \text{ and} \\
|\text{DS}_2(t)\rangle &= \hat{\mathcal{R}}[\alpha(t), \beta(t), 0]\,|F_g, -F_g\rangle.
\end{aligned} \tag{47}$$

The orthogonality of the instantaneous DS gives rise to exponentially in F_g supressed bit-flip error rates. This is because any fixed configuration of laser couplings with antipodal dark states is inherently bias preserving as per our analysis in the main text. A global SU(2) rotation of the frame does not change this property, provided the variation of the underlying laser couplings is sufficiently adiabatic. Note, after after simulating each gate operation via the colored noise master equation, we perform autonomous stabilization. To avoid excessive computation, we instead project the system into the subspace of driven-dissipative DSs directly as per Section IV.

A. $\hat{U}_{\tilde{z}}(\alpha_z)$ gate

We start with the single-qubit rotation $\hat{U}_{\tilde{z}}(\alpha_z) = \exp(-i\hat{\sigma}_{\tilde{z}}\alpha_z/2)$ for a fixed rotation angle α_z [not to be confused with the time-dependent laser parameter $\alpha(t)$]. The methodology for the gate is to adiabatically vary the direction of the DSs on the Bloch sphere [parametrized by the angles $\alpha(t)$, $\beta(t)$ from Eq. (45)] along a closed loop, as depicted in Main-text Fig. 2(b). The solid angle on the Bloch sphere enclosed by the loop sets the accrued phase and hence rotation angle α.

The specific laser ramp profile we choose, as a function of time $t \in [0, T]$ with T the total gate time, is given by,

$$\begin{aligned}
0 < t < \tfrac{T}{8}: \quad & \alpha(t) = 0 \\
& \beta(t) = \tfrac{\pi}{2} - \beta_1 \left[1 + \sin\left(4\pi \tfrac{t}{T} - \tfrac{\pi}{2}\right)\right] \\
\tfrac{T}{8} < t < \tfrac{T}{2}: \quad & \alpha(t) = \alpha_1 \cdot \tfrac{8}{3}\left(\tfrac{t}{T} - \tfrac{1}{8}\right) \\
& \beta(t) = \tfrac{\pi}{2} - \beta_1 \\
\tfrac{T}{2} < t < \tfrac{5T}{8}: \quad & \alpha(t) = \alpha_1 \\
& \beta(t) = \tfrac{\pi}{2} - \beta_1 \left[1 + \sin\left(4\pi \tfrac{t}{T} - \pi\right)\right] \\
\tfrac{5T}{8} < t < T: \quad & \alpha(t) = \alpha_1 \cdot -\tfrac{8}{3}\left(\tfrac{t}{T} - 1\right) \\
& \beta(t) = \tfrac{\pi}{2}
\end{aligned} \tag{48}$$

where $\alpha_1 = \frac{5\pi}{26}, \beta_1 = \frac{5\pi}{78}$ are fixed parameters. This profile yields a rotation angle $\alpha_z = 2F_g\alpha_1\cos(\frac{\pi}{2} - \beta_1)$. The profile is shown in main- text Fig.2(c).

Note that the PTM $\mathbf{R}$ for this gate operation is not diagonal. Ideally, it takes the form of,

$$\mathbf{R}_{\text{ideal}} = \begin{pmatrix} 1 & 0 & 0 & 0 \\ 0 & \cos(\alpha_z) & \sin(\alpha_z) & 0 \\ 0 & \sin(\alpha_z) & -\cos(\alpha_z) & 0 \\ 0 & 0 & 0 & 1 \end{pmatrix}. \tag{49}$$

In our simulations, we compute the "raw" PTM via the colored-noise simulations, multiply it by this ideal matrix $\mathbf{R} \to \mathbf{R}\mathbf{R}_{\text{ideal}}^{-1}$, and minimize the off-diagonal elements over all α_z (which amounts to correcting for deterministic under- or over-rotation, and can be corrected by adjusting the overall angle α_z of the gate). The remaining diagonal elements characterize the unrecoverable error channel of the gate, and are reported in main- text Fig. 3(c).

One can also add a counter-diabatic Hamiltonian $\hat{H}_{\text{CD}}(t)$ to compensates for the rapid driving by effectively cancelling the non-adiabatic transitions [14].

$$\hat{H}_{\text{CD}}(t)/\hbar = i \sum_{n=1,2} \left(|\partial_t \text{DS}_n(t)\rangle \langle \text{DS}_n(t)| - \langle \text{DS}_n(t)| \partial_t \text{DS}_n(t)\rangle |\text{DS}_n(t)\rangle \langle \text{DS}_n(t)|\right) \tag{50}$$

where $|\text{DS}_n(t)\rangle$ are the instantaneous eigenstates of the Hamiltonian $\hat{H}_{\text{DS}}(t)$, defined in Eq. (47). For the $\hat{U}_{\tilde{z}}(\alpha_z)$ gate, we can add a linear combination of $\hat{F}_{g,x}, \hat{F}_{g,y}, \hat{F}_{g,z}$ drive to actively rotate the $|\tilde{0}\rangle$, $|\tilde{1}\rangle$ logical states to make sure it follows the adiabatic loop.

$$\begin{aligned}
0 < t < \tfrac{T}{8}: \quad & \hat{H}_{\text{CD}}(t) = \dot{\beta}(t)\hat{F}_{g,y} \\
\tfrac{T}{8} < t < \tfrac{T}{2}: \quad & \hat{H}_{\text{CD}}(t) = \cos(\alpha(t))\sin(\beta_1)\cos(\beta_1)\dot{\alpha}(t)\hat{F}_{g,x} \\
& \quad + \sin(\alpha(t))\sin(\beta_1)\cos(\beta_1)\dot{\alpha}(t)\hat{F}_{g,y} + \sin(\alpha(t))\cos(\beta_1)\dot{\alpha}(t)\hat{F}_{g,z} \\
\tfrac{T}{2} < t < \tfrac{5T}{8}: \quad & \hat{H}_{\text{CD}}(t) = \dot{\beta}(t)\hat{F}_{g,x} \\
\tfrac{5T}{8} < t < T: \quad & \hat{H}_{\text{CD}}(t) = \dot{\alpha}(t)\hat{F}_{g,z}
\end{aligned} \tag{51}$$

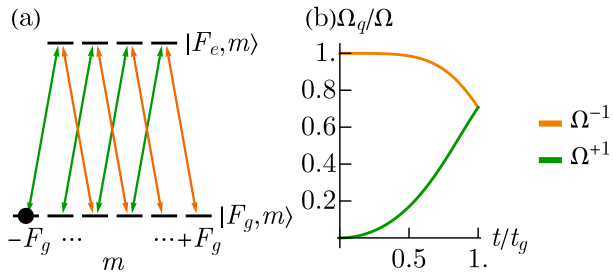

FIG. 5. (a) Schematic of the lasers and states used for preparation of the logical $|\widetilde{+}\rangle = (|\widetilde{0}\rangle + |\widetilde{1}\rangle)/\sqrt{2}$ state, starting from a spin-polarized $|F_g, -F_g\rangle$ atom. (b) Laser ramp profile for state preparation.

This profile transforms the approximate adiabatic solution into the exact solution of time dependent Schrödinger equation.

Note, the instantaneous counter-diabatic terms, which cancel the diabatic terms, are always orthogonal to the instantaneous axis defining the SCS. Thus, there exists a spatial rotation (around the SCS encoding axis) for which diabatic corrections act like an additional magnetic field.

B. $\hat{U}_{\widetilde{x}}$ gate

Next we consider a $\hat{U}_{\widetilde{x}} = \exp(-i\pi\hat{\sigma}_{\widetilde{x}})$ operation. This is straightforward to accomplish, as it amounts to rotating the state by π along the equator of the Bloch sphere, or equivalently swapping the $|\widetilde{0}\rangle$, $|\widetilde{1}\rangle$ logical states. One can accomplish the former by simply time-varying the laser couplings as,

$$0 < t < T: \quad \alpha(t) = \pi\, t/T, \text{ and } \beta(t) = \pi/2 \tag{52}$$

which corresponds to $\Omega^x(t) = \Omega\cos(\pi t/T)/\sqrt{2}$, $\Omega^y(t) = \Omega\sin(\pi t/T)/\sqrt{2}$ as shown in the main- text Fig. 2(c). The fidelity performance of this gate is similar to that of the $\hat{U}_{\widetilde{z}}(\alpha_z)$ gate, hence we do not provide explicit benchmarks. Furthermore, this gate can also be implemented digitally by an exchange of the $\{|\widetilde{0}\rangle, |\widetilde{1}\rangle\}$ logical states for the corresponding qubit. Doing so avoids the need for explicit (potentially faulty) quantum operations.

Similar to the $\hat{U}_{\widetilde{z}}$ gate, one can add a counter-adiabatic Hamiltonian

$$0 < t < T: \quad \hat{H}_{\text{CD}} = \dot{\alpha}(t)\hat{F}_{g,z} \tag{53}$$

to speed up the gate.

C. State preparation

Next we describe the preparation of a qubit into a logical state $|\widetilde{+}\rangle = (|\widetilde{0}\rangle + |\widetilde{1}\rangle)/\sqrt{2}$. The protocol starts by preparing a state in a maximally polarized state of the qubit hyperfine manifold $|\psi_g\rangle = |F_g, -F_g\rangle$ along the magnetic quantization axis. Atoms can be loaded into such a state with standard optical-pumping techniques.

We then turn the circular-polarized lasers $\Omega^{-1}(t)$ and $\Omega^{+1}(t)$ on, as depicted in Fig. 5(a). The time-dependent profile of the lasers is chosen analogous to a STIRAP protocol, where the laser that does not couple to the initially-populated state $|F_g, -F_g\rangle$ is turned on first. Fig. 5(b) shows the time-dependence of the laser couplings,

$$\begin{aligned} \Omega^{-1}(t) &= \Omega\frac{1+\cos\theta(t)}{\sqrt{2(1+\cos^2\theta(t))}}, \\ \Omega^{+1}(t) &= -\Omega\frac{1-\cos\theta(t)}{\sqrt{2(1+\cos^2\theta(t))}}, \end{aligned} \tag{54}$$

where in our simulations $\theta(t) := \frac{\pi}{2}\frac{t}{T}$ with $t = 0$ to preparation time T. During this adiabatic process, the two non-orthogonal SCSs stabilized by the system are

$$|\text{SCS}_1\rangle = |\pi - \theta(t), 0\rangle, \quad |\text{SCS}_2\rangle = |\pi - \theta(t), \pi\rangle. \tag{55}$$

So at time T the state we prepare will be a superposition of $|\widetilde{0}\rangle$ and $|\widetilde{1}\rangle$. Further, from the parity consideration the final state will be $|\widetilde{+}\rangle = (|\widetilde{0}\rangle + |\widetilde{1}\rangle)/\sqrt{2}$ given sufficient adiabaticity of the evolution.

Note that for this operation we directly report the fidelity rather than the PTM in the main-text Fig.3(d), as such matrix elements can exhibit ambiguity depending on the ramping state preparation protocol, since the operation extends outside the logical subspace. The master equation is otherwise solved in the same way as before, also employing colored noise with $N_X = 3$.

D. $\hat{\mathrm{C}}_X$ entangling gate

Here we detail the numerical simulation used to benchmark the $\hat{\mathrm{C}}_X$ gate implemented via the Rydberg blockade mechanism. As described in the main-text, the $\hat{\mathrm{C}}_X$ gate operation involves two atoms labeled control (C) and target (T). The control and target atom's logical qubit states are considered to be encoded x-axis within the F_g manifold of states, see main-text equation (2). The F_g manifold of state is laser-coupled to a Rydberg manifold of states $|F_r, m\rangle_{\mathrm{T}}$, with $m \in \{-F_r \ldots F_r\}$ and $F_r = F_g - 1$. The laser coupling is performed for the control and target in a resonant and off-resonant fashion, respectively and results in a controlled Pauli $\widetilde{x}$ rotation of the target atom, see main-text figure 4.

The selective resonant excitation of the control atom can, for instance, be performed by first adiabatically changing the drive parameters of H_{DS} for the control atom, such that the two DS can be identified with the two SCS $|\widetilde{0}\rangle_{\mathrm{C}} = |F_g,\, F_g\rangle_{\mathrm{C}}$ and $|\widetilde{1}\rangle_{\mathrm{C}} = |F_g,\, -F_g\rangle_{\mathrm{C}}$ from which a resonant excitation can be performed, see main-text figure 4(a) upper panel. The adiabatic change of driving parameters is described by Eq.(44) and (45) and can, for instance, be chosen as following

$$\begin{aligned} &\alpha(t) = 0 \\ &\beta(t) = \pi/2(1 - t/T). \end{aligned} \tag{56}$$

This choice ensures the two SCSs as the instantaneous DS are always antipodal with each other on the generalized Bloch sphere, which keeps the maximum separation and thus suppresses bit-flip errors and makes the adiabatic process biased, see Sec. V. Note that such an encoding is sensitive to dephasing from, *e.g.* magnetic field fluctuations, but nevertheless robust against bit-flip error, thus, bias preserving. We consider the logical state $|\widetilde{1}\rangle_{\mathrm{C}}$ to be resonantly excited to the Rydberg state $|F_r,\, -F_r\rangle_{\mathrm{C}}$, therefore, we henceforth call $|\widetilde{0}\rangle_{\mathrm{C}}$ and $|F_r,\, -F_r\rangle_{\mathrm{C}}$ the logical states of the control atom. Note, rotating the control qubit frame before exciting to a Rydberg state is not mandatory. One could instead directly implement a laser pulse of fixed circular polarization under a different axis of quantization, which can also perform the desired excitation.

Both the control and target Rydberg states can undergo decay due to spontaneous emission at rate γ_r. Decay of the target atom is incorporated into the simulations presented in the main-text (under the assumption that the atom decays back to the qubit manifold). Decay of the control atom is neglected in this simplified benchmark, although we provide a more careful treatment which includes it in the next section of the appendix.

The gate-operation simulations presented in the main-text underlie the following Lindblad master equation,

$$\hbar\frac{d}{dt}\hat{\rho}(t) = -i[\hat{H}_{\mathrm{Laser}} + \hat{H}_{\mathrm{Rydberg}},\, \hat{\rho}(t)] + \hbar\gamma_r \sum_{q=0,\pm1} \mathcal{D}\left[\sum_{m=-F_r}^{F_r} \mathcal{C}_{F_g,m;1,q}^{F_r,m+q}\, |F_g, m-q\rangle_{\mathrm{T}}\langle F_r, m|\right]\rho, \tag{57}$$

The coherent Hamiltonian $\hat{H}_{\mathrm{Laser}}$ contains the laser driving terms addressing the target qubit,

$$\hat{H}_{\mathrm{Laser}}/\hbar = \frac{1}{2}\sum_{q=0,\pm1}\left(e^{iq\Delta_r t}\,\Omega_r^q\,\hat{\mathcal{C}}_q^r + \mathrm{h.c.}\right), \tag{58}$$

with $\hat{C}_q^r = \sum_m \mathcal{C}_{F_g,m;1,q}^{F_r,m+q} |F_r, m+q\rangle_C\langle F_g, m|$, equal laser Rabi frequencies $\Omega_r^{+1} = \Omega_r^{-1} = \Omega_r$, and equal-and-opposite Rydberg laser detunings Δ_r. The second part of the Hamiltonian is the Rydberg-Rydberg interaction,

$$\hat{H}_{\mathrm{Rydberg}}/\hbar = V\,|F_r,\, -F_r\rangle_{\mathrm{C}}\langle F_r,\, -F_r| \otimes \sum_{m=-F_r}^{F_r} |F_r,\, m\rangle_{\mathrm{T}}\langle F_r,\, m|\,, \tag{59}$$

which we assume to be a diagonal uniform density shift with strength V. For simplicity, we solve just this master equation without factoring in field noise via colored noise simulations. Note for the simulations presented in the main-text we use $\gamma_r/\Omega_r = 2\pi/120$, which corresponds to a Rydberg lifetime of $1/\gamma_r = 40\,\mu s$ for $\Omega_r = 2\pi \times 3\,\mathrm{MHz}$.

The main-text Fig. 4 shows the time-evolution of different initial states under this master equation from time $t = 0$ to T with T the gate time. After all operations, we assume that dissipative stabilization is applied by projecting the qubit manifold into the logical basis following Section IV. The predicted gate time, as in the main-text, is $T = \pi/\mu$ with the effective rotation strength strength of,

$$\mu = \frac{|\Omega_r|^2}{4\Delta_r}\frac{1}{F_g}\frac{2F_g - 1}{2F_g + 1}. \tag{60}$$

Note however that the optimal fidelity may be at a time T_{opt} slightly different from π/μ due to e.g. effects from finite detuning Δ_r. This shift can be accounted via experimental calibration. Furthermore, instead of quenching on a constant laser coupling strength Ω_r, we ramp it on with the following profile

$$\Omega_r(t) = \Omega_r\left[\frac{1}{2} + \frac{\tanh(a\cos(\pi(2t/T - 1)^n))}{2\tanh(a)}\right], \tag{61}$$

where $a = 5$, $n = 4$, which helps to suppress left-over Rydberg population of the control atom.

We note that in general, while finite detuning from the target Rydberg state Δ_r causes error due to left-over Rydberg population, this detuning can be relatively small (e.g. $\Delta_r/\Omega_r \sim 10$) while still permitting fidelities on the order of $\sim 10^{-3}$. While the raw infidelity associated with finite Δ_r scales as $\sim \Omega_r^2/\Delta_r^2$, since this is a coherent error, it can be significantly mitigated by tailoring the gate times and/or laser ramp profiles such as the one above. In contrast, error caused by finite Rydberg interaction strength V/Δ_r (creating undesired rotation of the target) will scale as $\sim \Delta_r^2/V^2$, and cannot be as easily mitigated. For this reason we ideally we require Rydberg interaction strengths on the order of $V/\Delta_r \sim 100$ to e.g. reach the same $\sim 10^{-3}$ error thresholds that one can attain with finite detuning $\Delta_r/\Omega_r \sim 10$.

Finally, we comment that the gate assumes the control and target atoms to be close for strong Ry-Ry blockade V, but only the target atom is addressed by off-resonant lasers. Naively this requires tight focusing of beams addressing the target atom (to avoid cross-talk affecting the control), which can pose experimental challenges and limitations. Certain techniques can be used to avoid such limitations. Specifically, we assume that the control and target atom are excited to different Ry states. The control is resonantly excited to one Ry state if in logical $|\tilde{1}\rangle$ before the gate starts (after which, the target is moved closer to be in blockade range). The target is then off-resonantly coupled to a second Ry state during the gate. This prevents the control's Ry state from being coupled to by the target's beams.

One can still have cross-talk if the control is in logical $|\tilde{0}\rangle$, hence not Ry-excited and affected by the target's beams, causing it to experience some unwanted rotation. This cross-talk can be mitigated without requiring tightly focusing beams with a variety of ways:

- The control atom's logical $|\tilde{0}\rangle$ can likewise be "shelved" into a metastable state rather than a Ry-excited one before the target is driven. This shelving can also be done in a bias-preserving manner with a suitable choice of manifold and polarization control.

- Dynamical decoupling techniques can be used to cancel out unwanted rotation of the control atom (but not the target atom). For instance, one could slightly shift the position of the control atom optical tweezer, to change the phase of the one of the lasers addressing it by π, and hence flipping the sign of its effective magnetic field, but not the target's (see e.g. Ref. [15]).

- Dual-species encodings of different qubits can also in principle be utilized, for which operations affecting one atom but being off-resonant with the other can be implemented naturally [16].

E. Control atom decay correction

In this section we introduce a protocol for the $\hat{\mathrm{C}}_X$ gate to correct non-bias preserving processes due to control atom decay from the Ry state, which extends the discussion of the prior section. In particular, here we include decay of the control atom, assume that both atoms' Rydberg states decay into an independent ground state rather than the qubit manifold and provide a means of correcting control atom decay by monitoring the ground state population.

The Hilbert space we consider for the protocol is shown in Fig 6(a). The target atom still consists of a ground and Rydberg manifold $|F_g, m\rangle_{\mathrm{T}}$ and $|F_r, m\rangle_{\mathrm{T}}$, respectively, but now also an additional ground state $|g\rangle_{\mathrm{T}}$ into which the Rydberg state decays. The (hyper-)fine structure of this additional ground state is not tracked. Moreover, the control atom likewise has qubit and Rydberg states $|\tilde{0}\rangle_{\mathrm{C}}$ and $|F_r, -F_r\rangle_{\mathrm{C}}$, as well as a ground state $|g\rangle_{\mathrm{C}}$. The laser coupling Hamiltonian $\hat{H}_{\text{Laser}}$ and the Rydberg-Rydberg interaction $\hat{H}_{\text{rydberg}}$ remain the same, but the master equation is adjusted to be

$$\hbar\frac{d}{dt}\rho = -i[\hat{H}_{\text{laser}} + \hat{H}_{\text{rydberg}}, \rho] + \hbar\gamma_r\mathcal{D}[|g\rangle_{\mathrm{C}}\langle F_r, -F_r|]\rho + \hbar\gamma_r\sum_{m=-F_r}^{F_r}\mathcal{D}[|g\rangle_{\mathrm{T}}\langle F_r, m|]\rho. \tag{62}$$

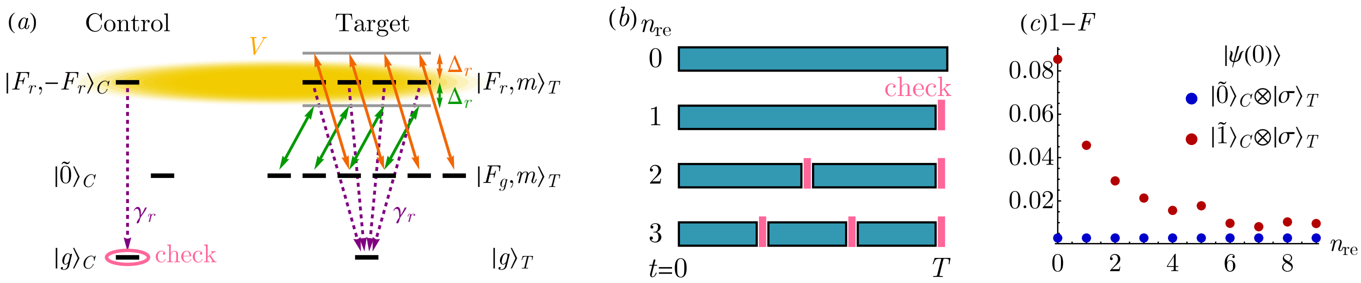

FIG. 6. (a) Schematic of the Hilbert space used for numerical simulation of the bias-preserving $\hat{\mathrm{C}}_X$ gate with more careful accounting of Rydberg decay due to spontaneous emission. (b) Schematic of the monitoring protocol that makes $n_{\rm re}$ checks of the $|g\rangle_{\rm C}$ population during the gate to detect control Rydberg decay. (c) Bit-flip infidelity of the gate, depending on whether the control atom starts in $|\widetilde{0}\rangle_{\rm C}$ or $|\widetilde{1}\rangle_{\rm C}$ (the latter corresponds to $|F_r, -F_r\rangle_{\rm C}$). We vary the number $n_{\rm re}$ of checks for control atom decay. The parameters used are $F_g = 4$, $\Delta_r/\Omega_r = 2$, $\gamma_r/\Omega_r = 2\pi/120$, and $V/\Omega_r = 100$. Note that during each interval we use a constant Rabi frequency Ω_r (rather than the ramp in the previous section) for simplicity.

With control atom decay incorporated, we observe that if such a decay happens during gate execution, Rydberg blockade will cease and the target will start to rotate, which can cause non-negligible bit-flip error. To mitigate this effect, we can adjust our gate protocol to include a monitoring process. This adjusted protocol periodically checks whether the control atom decayed during the gate time by measuring the ground state.

The protocol proceeds by splitting the full gate time T into $n_{\rm re}$ equal subintervals of length $T/n_{\rm re}$ indexed by $n \in \{1, 2, \ldots n_{\rm re}\}$, as depicted in Fig. 6(b). At the end of each subinterval, we check if Rydberg decay of the control has occurred by projectively measuring the population of $|g\rangle_{\rm C}$. The case $n_{\rm re} = 0$ means we don't perform any checks. If the control atom is detected in the ground state after a given check, it should have been in the Rydberg state and thus blockading rotation of the target. Upon such detection we stop the gate operation early (turn off the lasers addressing the target) to prevent further unwanted rotation. If no decay was detected, the gate continues to the next subinterval. At the end of the gate we assume that any direct population outside the target's qubit manifold is lost, then finally we apply dissipative stabilization.

For simplicity, to benchmark this augmented protocol we simply compute the gate fidelity for certain initial states. The initial condition we take for the gate evolution is a pure state,

$$|\psi(0)\rangle = |\sigma'\rangle_{\rm C} \otimes |\sigma\rangle_{\rm T}\,, \tag{63}$$

with $\sigma, \sigma' \in \{\widetilde{0}, \widetilde{1}\}$, noting that here $|\widetilde{1}\rangle_{\rm C} = |F_r, -F_r\rangle_{\rm C}$.

The ideal final state after the gate operation $|\psi_{\rm ideal}\rangle$ depends on whether the control was Rydberg blockading or not:

$$|\psi_{\rm ideal}\rangle = \begin{cases} |\widetilde{1}\rangle_{\rm C} \otimes |\sigma\rangle_{\rm T}\,, & |\psi(0)\rangle = |\widetilde{1}\rangle_{\rm C} \otimes |\sigma\rangle_{\rm T} \\ |\widetilde{0}\rangle_{\rm C} \otimes |\overline{\sigma}\rangle_{\rm T}\,, & |\psi(0)\rangle = |\widetilde{0}\rangle_{\rm C} \otimes |\sigma\rangle_{\rm T} \end{cases} \tag{64}$$

where $\overline{\widetilde{0}} = \widetilde{1}$, $\overline{\widetilde{1}} = \widetilde{0}$. The fidelity is obtained via,

$$F = \mathrm{tr}\left[\rho_f \cdot |\psi_{\rm ideal}\rangle \langle \psi_{\rm ideal}|\right]. \tag{65}$$

In Fig 6(c) we plot the resulting fidelity for different numbers of checks $n_{\rm re}$. If the control starts in $|\widetilde{0}\rangle_{\rm C}$, there is no Rydberg blockade or decay. The fidelity only depends on Ω_r/Δ_r, approaching $F = 1$ in the limit $\Omega_r/\Delta_r \to 0$ (for which adiabatic elimination of the target Rydberg state is perfect). On the other hand, if the control starts in $|r\rangle_{\rm C}$, the fidelity starts out poor due to Rydberg decay of the control, but improves exponentially in the number of checks $n_{\rm re}$, approaching the fidelity of the non-blockaded case in the limit $n_{\rm re} \to \infty$. Note, the non-monotonic behavior occurs due to finite detuning Δ_r causing target Rydberg state population oscillations. Crucially, these simulations show that with only a few checks, the effective bit-flip fidelity can be greatly decreased.

This augmented procedure does not correct for phase-flip error, which will generally occur at rate $\sim 1 - \exp(-\gamma_r T) \sim \gamma_r T$ (for $\gamma_r T \ll 1$). However, this type of error can still be rendered small with longer-lived Rydberg states and shorter gate times. Reduction of the bit-flip fidelity compared to the phase-flip also remains favorable for biased error correction protocols.

VI. NON-BIAS-PRESERVING GATES: UNIVERSALITY ON THE PHYSICAL QUBIT LEVEL

As a supplement, in this section we provide several gate designs for the dark spin-cat encoding, which could be more native but lose the bit-flip protection. We first explain the collision-and-expansion trick and how to use this for the $\hat{U}_{\widetilde{x}}(\alpha_x)$ gate design,

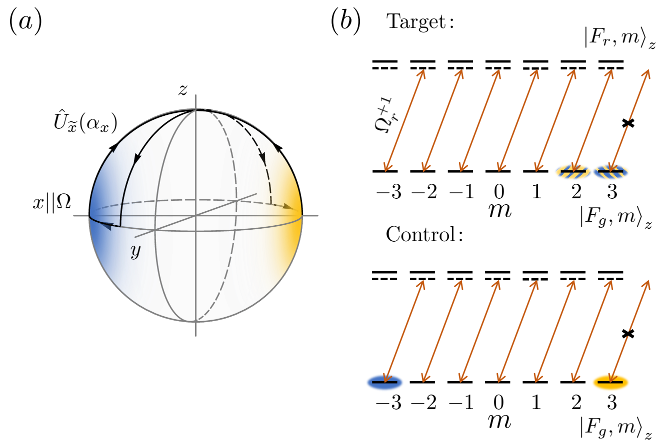

FIG. 7. Schematic plot for native non-bias-preserving gate design. (a) The path of two SCSs during $\hat{U}_{\tilde{x}}(\alpha_x)$ gate execution. They first collide and then separate in another direction. (b) The entangling operation in the middle of the native $\hat{C}_X$ execution. For the target atom, the collision step will convert $|\tilde{+}\rangle$ to $|F_g, F_g\rangle_z$ and $|\tilde{-}\rangle$ to $|F_g, F_g-1\rangle_z$.

which is inspired by the bosonic-cat code gate construction as proposed in Ref. [17]. This gate does not preserve the error bias as we have to reduce the spatial separation for the two SCSs on the generalized Bloch sphere in order to exchange the population between $|\tilde{0}\rangle$ and $|\tilde{1}\rangle$ code states. This gate, together with 1-qubit $\hat{U}_{\tilde{z}}(\alpha_z)$ and entangling $\hat{C}_Z$ operation, which we discussed before, complete a universal gate set on the physical encoding level. Additionally, in the second part of the section, we discuss a simplified non-bias-preserving construction of the $\hat{C}_X$ gate using the collision-and-expansion trick.

Here are two things that we would like to point out. First, in principle, those unbiased gates are not strictly necessary, as the bias-preserving gate set shown in the main text (including $\hat{C}_X$ and Toffoli) are universal for fault-tolerant operations logical (repetition code) qubits [18]. Nevertheless, those non-bias-preserving constructions can still offer sufficient advantages when the performance of bias-preserving $\hat{C}_X$ gates is limited. For example, neutral atom quantum processors exhibit negligible 1-qubit gate infidelities as compared to the $\hat{C}_Z$ gate performance, which is limited by Rydberg decay. However, Ref. [19] pointed out that, if it is possible to detect the location of the decay event and supply a fresh atom initialized in $|1\rangle$ (since only $|1\rangle$ is excited to the Rydberg state), it is convertable to a dephasing error with known location. This so-called "biased-erasure" error during $\hat{C}_Z$ implementation provides an error correction threshold around 10% without the need of bias-preserving $\hat{C}_X$ gate, and can be even higher exploiting ideas presented in [19]. As explained in the main text, our dark spin-cat encoding can be well adapted to this framework.

A. Holonomic 1-qubit $\hat{U}_{\tilde{x}}(\alpha_x)$ gate

In this section, we briefly present how to construct a single-qubit $\hat{U}_{\tilde{x}}(\alpha_x)$ gate by adiabatically changing the driving parameters $\Omega_{\pm 1}(t)$. We start with $\Omega_{+1} = -\Omega_{-1} = \Omega$, such that the code subspace is spanned by $\{|F_g, F_g\rangle_x, |F_g, -F_g\rangle_x\}$, *i.e.* two SCSs pointing along the x-axis on the generalized Bloch sphere. We first adiabatically reduce the amplitude Ω_{-1} to 0 in order to collide the two SCSs at the north pole of the generalized Bloch sphere. Then, we separate them in another direction by adiabatically increasing Ω_{-1} to $-\Omega e^{-2i\alpha_x}$, and finally changing Ω_{-1} to $-\Omega$ without affecting its amplitude. The location change for the two SCSs during the whole process is illustrated in Fig. 7(a).

Note, in the absence of the Ω_0 drive, one of the dark states lies in the subspace spanned by $\{|F_g, F_g-2k\rangle_z\}$ while another one is in the subspace spanned by $\{|F_g, F_g-(2k+1)\rangle_z\}$. Therefore, during the first step where we adiabatically turn off Ω_{-1}, the state $\frac{1}{\sqrt{2}}(|F_g, F_g\rangle_x + e^{2i\pi F_g}|F_g, -F_g\rangle_x)$ connects to $|F_g, F_g\rangle_z$, while $\frac{1}{\sqrt{2}}(|F_g, F_g\rangle_x - e^{2i\pi F_g}|F_g, -F_g\rangle_x)$ is connected to $|F_g, F_g-1\rangle_z$. Following the convention in Ref. [17], we denote this mapping as $S_0^\dagger$, Due to the rotational symmetry in the system the operation for the second step is S_{α_x}, which is related to S_0 by a rotation operator $S_{\alpha_x} = \mathcal{R}(\alpha_x, 0, 0)S_0\mathcal{R}^\dagger(\alpha_x, 0, 0)$. The third step is simply a rotation $\mathcal{R}^\dagger(\alpha_x, 0, 0)$. The whole process leads to an operation $\mathcal{R}^\dagger(\alpha_x, 0, 0)S_{\alpha_x}S_0^\dagger = S_0\mathcal{R}^\dagger(\alpha_x, 0, 0)S_0^\dagger$ on the dark-state subspace. Therefore, $\frac{1}{\sqrt{2}}(|F_g, F_g\rangle_x + e^{2i\pi F_g}|F_g, -F_g\rangle_x)$ will pick up a $e^{i\alpha_x F_g}$ phase while $\frac{1}{\sqrt{2}}(|F_g, F_g\rangle_x + e^{2i\pi F_g}|F_g, -F_g\rangle_x)$ will get a phase of $e^{i\alpha_x(F_g-1)}$. As a result, an arbitrary superposition of the two code states will become the following state after the whole process

$$c_+\frac{|\widetilde{0}\rangle + e^{2i\pi F_g}|\widetilde{1}\rangle}{\sqrt{2}} + c_-\frac{|\widetilde{0}\rangle - e^{2i\pi F_g}|\widetilde{1}\rangle}{\sqrt{2}} \longrightarrow e^{i\alpha_x F_g}\left[c_+\frac{|\widetilde{0}\rangle + e^{2i\pi F_g}|\widetilde{1}\rangle}{\sqrt{2}} + c_- e^{-i\alpha_x}\frac{|\widetilde{0}\rangle - e^{2i\pi F_g}|\widetilde{1}\rangle}{\sqrt{2}}\right], \tag{66}$$

which corresponds to $\hat{U}_{\widetilde{x}}(\pm\alpha_x)$ for a half-integer / integer F_g. This operation, together with $\hat{U}_{\widetilde{z}}(\alpha_z)$ gate, provides arbitrary 1-qubit rotation on the dark spin-cat encoding.

The $\hat{U}_{\widetilde{x}}(\alpha_x)$ gate in general does not preserve the Pauli error bias. It will convert part of the Z error before the gate to the Y error when α_x is not an integer multiple of π. This can also be viewed from the trajectories of the two SCSs during the gate execution, as their collision will lead to the population exchange between computational basis states and convert phase-flip error to bit-flip. As a result, the $\hat{\mathrm{C}}_X$ implementation involving the use of such $\hat{U}_{\widetilde{x}}(\alpha_x)$ gate does not preserve the Pauli error bias.

B. Native implementation for non-bias-preserving $\hat{\mathrm{C}}_X$ gate

With arbitrary 1-qubit rotations and the $\hat{\mathrm{C}}_Z$ entangling gate, we can achieve universal operations on the physical encoding level, including the $\hat{\mathrm{C}}_X$ operations as $\hat{\mathrm{C}}_X = \hat{U}_{\widetilde{y},T}(\frac{\pi}{2})\hat{\mathrm{C}}_Z\hat{U}_{\widetilde{y},T}(-\frac{\pi}{2})$. However, we can further simplify the $\hat{\mathrm{C}}_X$ control sequence in a more native manner using the collision-and-expansion trick we introduced in the $\hat{U}_{\widetilde{x}}(\alpha_x)$ gate construction.

We briefly explain the idea as follows. The first step is again converting the encoding from Fock states in x basis to Fock in z basis, but for the control and target atom the protocol is different. For the control atom, the conversion protocol can be the same as that used for the control atom in bias-preserving $\hat{\mathrm{C}}_X$ or $\hat{\mathrm{C}}_Z$ construction shown in the main text, i.e., adiabatically transfer $|\widetilde{0}/\widetilde{1}\rangle = |F_g, \pm F_g\rangle_x$ to $|F_g, \pm F_g\rangle_z$ while always keeping them antipodal during the evolution. On the other hand, for the target atom we can use the collision trick that converts $|\widetilde{+}\rangle$ to $|F_g, F_g\rangle_z$ and $|\widetilde{-}\rangle$ to $|F_g, F_g-1\rangle_z$ by adiabatically turning off the Ω_{-1} drive [20].

After the conversion above, we need to perform the entangling operation. Here we consider a Rydberg manifold with $F_r = F_g$. Consider using a σ_+ polarized drive to address the state from the encoded manifold to the Rydberg manifold. Due to the selectivity that comes from the polarization, $|F_g, F_g\rangle_z$ will not couple with the Rydberg levels, but $|F_g, -F_g\rangle_z$ and $|F_g, F_g-1\rangle_z$ will. Therefore, one can use the standard $\hat{\mathrm{C}}_Z$ control sequence [21] so that both $|F_g, F_g\rangle_{z,C} \otimes |F_g, F_g-1\rangle_{z,T}$ and $|F_g, -F_g\rangle_{z,C} \otimes |F_g, F_g\rangle_{z,T}$ will pick up a phase $e^{i\phi}$ while $|F_g, -F_g\rangle_{z,C} \otimes |F_g, F_g-1\rangle_{z,T}$ will get a phase $e^{i(2\phi-\pi)}$. This is equivalent to a $\hat{\mathrm{C}}_Z$ operation up to single-qubit phase rotations. Finally, we need to map the encoded subspaces from the Fock z basis back to the Fock x basis. We can choose a different trajectory compared with that used in the first step to account for the required extra 1-qubit gates. For the control atom, we still need to keep the two SCSs antipodal, which is similar to the idea used in $\hat{U}_{\widetilde{z}}(\alpha_z)$ gate construction. On the other hand, for the target atom, we can follow the 2nd and 3rd steps used in $\hat{U}_{\widetilde{x}}(\alpha_x)$ gate design. At the end of the protocol, only $|\widetilde{1}\rangle_C \otimes |\widetilde{-}\rangle_T$ will get a relative π phase, which results in a $\hat{\mathrm{C}}_X$ gate.

Finally, we would like to point out that this simplified version of $\hat{\mathrm{C}}_X$ execution can still be adapted to the "biased-erasure" framework, provided that the error from 1-qubit control is negligible and the Rydberg decay during entangling operations can be detected. If the decay is detected on the control atom, we prepare a fresh $|\widetilde{1}\rangle$, and if it is on the target atom we prepare a fresh $|\widetilde{-}\rangle$. In this way, we again have the knowledge about both the location and the type of the error (for the control atom the error is Z type, while for the target it is X type). This noise pattern is equivalent to the $\hat{\mathrm{C}}_X = \hat{U}_{\widetilde{y},T}(\frac{\pi}{2})\hat{\mathrm{C}}_Z\hat{U}_{\widetilde{y},T}(-\frac{\pi}{2})$ construction proposed in [19] where the error during $\hat{\mathrm{C}}_Z$ in the middle is biased-erasure that both the control and target will have Z type of error after erasure conversion. Z error on the target will be converted to X error after $\hat{U}_{\widetilde{y},T}(\frac{\pi}{2})$ rotation, which leads to the same error structure for the $\hat{\mathrm{C}}_X$ construction as we proposed here.

[1] B. King, arXiv:0804.4528 (2008).
[2] J. J. Sakurai and J. Napolitano, *Modern quantum mechanics* (Cambridge University Press, 2020).
[3] J. R. Morris and B. W. Shore, Phys. Rev. A **27**, 906 (1983).
[4] J. M. Radcliffe, J. Phys. A: Gen. Phys. **4**, 313 (1971).
[5] P. Zoller, G. Alber, and R. Salvador, Phys. Rev. A **24**, 398 (1981).
[6] N. G. Van Kampen, Physics reports **24**, 171 (1976).
[7] C. Gardiner, *Stochastic methods*, Vol. 4 (Springer Berlin, 2009).
[8] D. W.-C. Miao, Appl. Probab. **50**, 1102 (2013).
[9] M. Am-Shallem, A. Levy, I. Schaefer, and R. Kosloff, arXiv:1510.08634 (2015).
[10] S. Roncallo, L. Maccone, and C. Macchiavello, Quantum Sci. Technol. **9**, 015010 (2023).

[11] I. I. Sobelman, *Introduction to the theory of atomic spectra: International series of monographs in natural philosophy*, Vol. 40 (Elsevier, 2016).
[12] V. V. Albert, arXiv:1802.00010 (2018).
[13] A. Piñeiro Orioli, J. K. Thompson, and A. M. Rey, Physical Review X **12**, 011054 (2022).
[14] A. del Campo, Phys. Rev. Lett. **111**, 100502 (2013).
[15] A. L. Shaw, R. Finkelstein, R. B.-S. Tsai, P. Scholl, T. H. Yoon, J. Choi, and M. Endres, Nature Physics **20**, 195 (2024).
[16] S. Anand, C. E. Bradley, R. White, V. Ramesh, K. Singh, and H. Bernien, Nature Physics **20**, 1744 (2024).
[17] V. V. Albert, C. Shu, S. Krastanov, C. Shen, R.-B. Liu, Z.-B. Yang, R. J. Schoelkopf, M. Mirrahimi, M. H. Devoret, and L. Jiang, Phys. Rev. Lett. **116**, 140502 (2016).
[18] J. Guillaud and M. Mirrahimi, Phys. Rev. X **9**, 041053 (2019).
[19] K. Sahay, J. Jin, J. Claes, J. D. Thompson, and S. Puri, Physical Review X **13**, 041013 (2023).
[20] This convention applies when F_g is an integer. If F_g is a half-integer, then the protocol will map $|\widetilde{-}\rangle$ to $|F_g, F_g\rangle_z$ and $|\widetilde{+}\rangle$ to $|F_g, F_g - 1\rangle_z$.
[21] H. Levine, A. Keesling, G. Semeghini, A. Omran, T. T. Wang, S. Ebadi, H. Bernien, M. Greiner, V. Vuletić, H. Pichler, *et al.*, Phys. Rev. Lett. **123**, 170503 (2019).